 DOI: 10.17344/acsi.2016.2995 *Acta Chim. Slov.* **2017,** *64,* 170–178

Scientific paper

Nitrogen Doped Graphene Nickel Ferrite Magnetic Photocatalyst for the Visible Light Degradation of Methylene Blue

Rajinder Singh, Jigmet Ladol, Heena Khajuria and Haq Nawaz Sheikh*

Department of Chemistry, University of Jammu, Jammu Tawi,180 006 India

** Corresponding author: E-mail: hnsheikh@rediffmail.com*

Received: 14-10-2016

Abstract

A facile approach has been devised for the preparation of magnetic $NiFe_2O_4$ photocatalyst ($NiFe_2O_4$-NG) supported on nitrogen doped graphene (NG). The $NiFe_2O_4$-NG composite was synthesized by one step hydrothermal method. The nanocomposite catalyst was characterized by Powder X-ray diffraction (PXRD), Scanning electron microscopy (SEM), Transmission electron microscopy (TEM), Fourier transform infrared spectroscopy (FTIR), Ultraviolet–visible spectroscopy (UV-Vis) and Vibrating sample magnetometry (VSM). It is found that the combination of $NiFe_2O_4$ nanoparticles with nitrogen-doped graphene sheets converts $NiFe_2O_4$ into a good catalyst for methylene blue (MB) dye degradation by irradiation of visible light. The catalytic activity under visible light irradiation is assigned to extensive movement of photogenerated electron from $NiFe_2O_4$ to the conduction band of the reduced NG, effectively blocking direct recombination of electrons and holes. The $NiFe_2O_4$ nanoparticles alone have efficient magnetic property, so can be used for magnetic separation in the solution without additional magnetic support.

Keywords: Nanostructures, photodegradation, nickel ferrite, catalysts, absorption, UV/Vis spectroscopy.

1. Introduction

Photocatalysis especially by TiO_2 has been widely used for the purification of waste water. The energy band gap of 3.2 eV is required for the excitation of electron by light in TiO_2 catalyst so UV light can only be used in the process of photodegradation. The development of visible light sensitive photocatalysts by band gap modifications and external surface changing for waste water treatment and degradation of organic dye is an active area in photocatalysis.[1–7] Graphene has attracted the attention due to various applications.[8–11] Graphene has sp^2 hybridized carbon and one atom thick (2-D) sheet of conjugated system and extraordinary physical and chemical properties.[12–16] There has been so much focus to develop graphene-metal oxide photocatalysts such as TiO_2-graphene and ZnO-graphene for the photodegradation of organic dye by the irradiation of visible light.[17–22] The heterogeneous systems are mostly used to perform the photodegradation reactions. The repeated use of photocatalysts after degradation is of great importance for sustainable use of the catalyst. The magnetic nanoparticles anchored on solid support serve as heterogenous catalyst allowing facile separation of catalyst from reaction products.[23] Superparamagnetic copper ferrite-graphene nanocomposite prepared via hydrothermal method acts as excellent catalyst for the reduction of nitroarenes. The big advantage of the catalyst is that it can be easily recovered and retains the catalytic activity even after five catalytic cycles.[24] Copper–cobalt ferrites prepared by hydrothermal method from co-precipated precursor serve as efficient catalyst in the decomposition of methanol to CO and H_2.[25] The various metal ferrites have been used as catalysts in phenols decomposition, detoxification of CO gas from automobile exhaust, anodic material for lithium ion batteries.[26–29] Nickel ferrite ($NiFe_2O_4$) has the inverse spinel structure. The ferrimagnetism arises due to antiparallel spin of Fe^{3+} ions present at tetrahedral sites and Ni^{2+} occupying octahedral sites.[30] The Nickel ferrite is considered as the efficient magnetic material which has good electrical resistivity, high-Curie temperature and chemical stability. Magnetic nanoparticles of nickel ferrite have been used to manufacture titania-coated nickel ferrite, which can act as magnetically separable photocatalyst.[31] The TiO_2 doped $NiFe_2O_4$ nanopar-

ticles possess band gap of 2.19 eV and have displayed enhanced photocatalytic activity as compared to TiO_2 for degradation of Rhodamine B dye in aqueous solution under visible light irradiation.[32] Pure nickel ferrite is photo-catalytically inactive but its composite with another semiconductor (e.g., graphene sheets) can find an effective mechanism for separation of charges leading to increased photocatalytic performance. One such example is Zn-Fe_2O_4-graphene photocatalyst and its great performance in the photocatalytic degradation of MB under visible light irradiation.[33] Carbon material doped with a heteroatom, such as B, N or S, can increase the pseudo capacitance by manipulating its electronic properties and chemical reactivity leading to increased performance of doped grapheme.[34–37] Nitrogen-doped graphene (NG) has great utility because of its higher specific capacitance matched to the pristine graphene and good durability, therefore, enabling its use as electrode materials for supercapacitors and applications in photocatalysis.[38]

In this paper, we report the development of one step method to design magnetically separable nitrogen doped graphene-based photocatalyst having excellent catalytic activity. The approach is designed to deposit $NiFe_2O_4$ nanocrystals on nitrogen doped graphene sheets via a one-step hydrothermal method. Interestingly, in the presence of nitrogen doped graphene, the inert nanocrystals of Ni-Fe_2O_4 have been converted into a highly efficient catalyst for the methylene blue (MB) degradation under visible light irradiation. In addition, $NiFe_2O_4$ nanoparticles themselves have a magnetic property, which makes the Ni-Fe_2O_4–NG composite magnetically separable in liquid medium.

2. Experimental

2. 1. Materials

Iron(III) nitrate nonahydrate $Fe(NO_3)_3 \cdot 9H_2O$, Nickel(II) nitrate hexahydrate $Ni(NO_3)_2 \cdot 6H_2O$, graphite powder flakes, phosphoric acid and hydrogen peroxide were purchased from Alfa Aesar. All chemicals were used as received without further purification. Ethanol, urea, sodium hydroxide and sulphuric acid were purchased from Sigma Aldrich. Deionized water was used throughout.

2 .2. Synthesis of Magnetic $NiFe_2O_4$-Nitrogen Doped Graphene Composite Photocatalyst

Purified natural graphite was used for the synthesis of graphene oxide (GO) by the well known method given by Hummers and Offeman.[39] The graphene oxide (GO) (0.08 g) was dispersed in 20 ml of absolute ethanol and sonicated for 45 min. In a separate beaker 0.28 g of $Ni(NO_3)_2 \cdot 6H_2O$ and 0.78g of $Fe(NO_3)_3 \cdot 9H_2O$ mixture was added to 10 ml absolute ethanol with constant stirring for 30 min forming homogenous solution. The two solutions were mixed and pH of the mixture solution was kept 10.0 using 6 M NaOH solution and then 1 g urea was added into it. The resulting mixture was put into a 50 mL Teflon-lined stainless steel autoclave and heated to 180 °C for 18 h in an oven. After cooling the reaction mixture to room temperature and the precipitates were filtered, washed with distilled water and dried in oven at 70 °C for 12 h. The product was named as $NiFe_2O_4$–NG. Same method was applied to synthesize pure $NiFe_2O_4$ with the modification that GO and urea were excluded. Sulfur was estimated as $BaSO_4$ by gravimetric method and Chloride was estimated as AgCl by Volhard's method.[40]

2. 3. Spectroscopic and Microscopic Measurements

The phase and size of the as-prepared samples were determined from powder X-ray diffraction (PXRD) using D8 X-ray diffractometer (Bruker) at a scanning rate of 12° min^{-1} in the 2θ range from 10° to 70°, with Cu Kα radiation (λ = 0.15405 nm). Scanning electron microscopy (SEM) micrographs of the samples were recorded on FEI Nova Nano SEM 450. High Resolution Transmission Electron Microscopy (HRTEM) was recorded on Tecnai G2 20 S-TWIN Transmission Electron Microscope with a field emission gun operating at 200 kV. The samples for TEM measurements were prepared by evaporating a drop of the colloid onto a carbon coated copper grid. The infrared spectra were recorded on Shimadzu Fourier Transform Infrared Spectrometer (FT-IR) over the range of wave number 4000–400 cm^{-1} and the standard KBr pellet technique was employed. The magnetic moment as a function of applied field was recorded using Vibrating Sample Magnetometer (VSM), Lakeshore 7410. All the measurements were performed at room temperature.

2. 4. Photocatalytic Activity Measurement

The catalytic activity of the as synthesized sample was performed by degradation of organic dye MB under the irradiation of visible light. For the Photo irradiation 500 W xenon lamp was used fitted with UV cut-off filters (JB450) in order to completely remove any radiation below 420 nm ensuring the exposure to only visible light. The whole procedure was performed at 25 °C. A 100 mL of MB dye solution was prepared (20 mg/L concentration) and 0.025 g of photocatalyst was mixed with dye solution. The resulting mixture was stirred for 60 min before illumination in order to establish the adsorption – desorption equilibrium between MB and catalyst surface. At same instant of time 5 mL of dye-catalyst mixture was taken out and concentration of the residual dye was determined with the help of UV-vis spectroscopy by measuring the absorption at 664 nm. The absorbance of dye at 664 nm was monitored with time after fixed intervals of time. The absor-

bance of dye with time without catalyst was also recorded for reference.

3. Results and Discussion

3. 1. PXRD Measurements

The structural characterization of the nanoparticles has been carried out by Powder X-ray diffraction technique using Cu*K*α radiation. Figure 1(a–b) show the differences of phase composition between GO and NG. The doping of nitrogen in GO can be clarified easily by PXRD spectrum. The PXRD pattern of GO exhibits a characteristic (002) peak of graphite emerging at 24.2°. Compared with GO, it is found that the (002) peak of NG appears at 26.3` which indicates that nitrogen atoms have entered into the crystal lattice of graphite and caused the increased distance between the graphite layers. This confirms the formation of nitrogen-doped graphene by urea assisted hydrothermal reaction. Figures 1c, d show the PXRD diffraction patterns of the pure $NiFe_2O_4$ and as prepared $NiFe_2O_4$–NG. The diffraction peaks at 30.9°, 35.7°, 43.4°, 53.7°, 57.2° and 63.2° corresponding to the planes (220), (311), (400), (422), (511) and (440) are allocated to spinel-type $NiFe_2O_4$ (JCPDS No. 54–0964).[41] Similar diffraction patterns are observed for $NiFe_2O_4$–NG. The nitrogen doped graphene oxide can be reduced by the alcohol under hydrothermal conditions and no peak at (002) is observed in the composite. It can also be related to well exfoliation of the NG sheets in the resulting composite material. So the diffraction pattern of NG disappears in the XRD pattern of $NiFe_2O_4$–NG.

The average crystallite size of these nanoparticles was calculated according to the Scherrer's equation.

$$\beta = \frac{k\lambda}{LCos\theta} \quad (1)$$

where, L (nm) is the crystallite size, λ (nm) is the wavelength of the Cu Kα radiant, λ = 0.15405 nm, β(°) is the full-width at half-maximum (FWHM) of the diffraction peak, θ is the diffraction angle and *K* is the Scherrer constant equal to 0.89. All the major peaks were used to calculate the average crystallite size of the $NiFe_2O_4$ and $NiFe_2O_4$–NG nanoparticles. The estimated average crystallite sizes of nanoparticles are in the range of 80–120 nm.

3. 2. SEM and TEM Analysis

Figure 2a shows representative scanning electron microscopy and transmission electron microscopy images of the prepared GO. From the SEM image, morphology and structure of as-prepared graphene oxide sample was investigated. GO sheets were cast on a gold coated (100 nm) Si/SiO_2 substrate. It has been found that the graphene flakes have wrinkled surfaces. Furthermore, in the TEM image (Figure 3a) GO shows layer-by-layer stacked structure and has wrinkled paper like morphology. Such morphological changes can be attributed to the increased formation of phenolic and epoxy functional groups on the basal plane of GO. The curled and overlapped nanosheets can be clearly observed. The SEM image (Figure 2b) and TEM image (Figure 3b) reveal that nitrogen-doped grapene nanosheets exhibit a typical wrinkled structure, which results from stable bending thermodynamically.[42,43]

Figures 2(c–d) show SEM images of the $NiFe_2O_4$ and $NiFe_2O_4$–NG samples where as Figures 3(c–d) show TEM images of the $NiFe_2O_4$ and $NiFe_2O_4$–NG samples. In Figure 2c and Figure 3c, $NiFe_2O_4$ nanoparticles are clear-

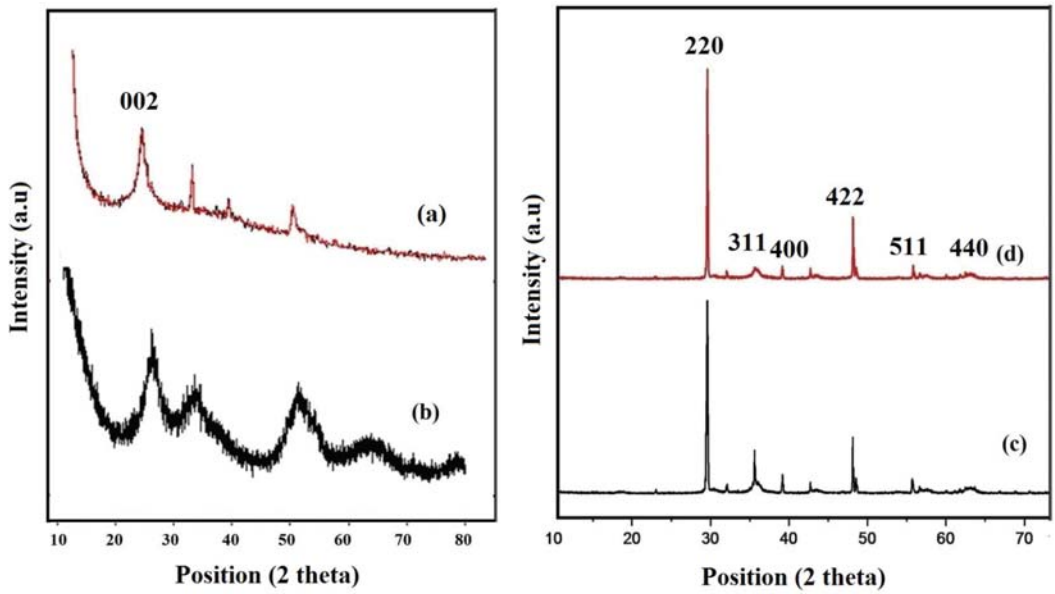

Figure 1. PXRD patterns of (a) GO, (b) NG, (c) $NiFe_2O_4$ and (d) $NiFe_2O_4$–NG.

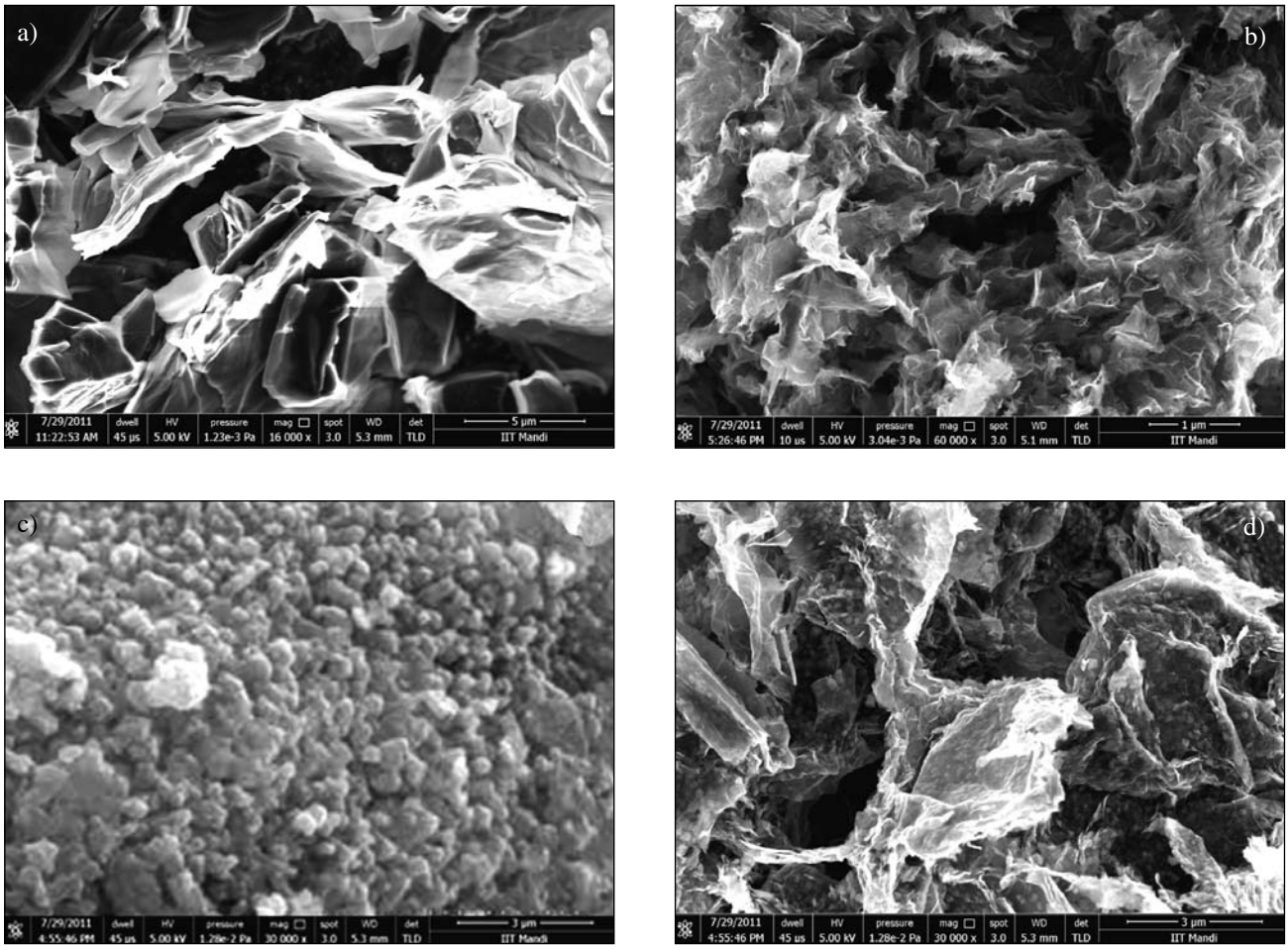

Figure 2. SEM images of (a) GO (b) NG (c) $NiFe_2O_4$ and (d) $NiFe_2O_4$–NG.

ly visible in the SEM and TEM images. The $NiFe_2O_4$ nanoparticles distributed on NG to form nanoparticles bound on the surface of NG sheets is seen in the Figure 2d and Figure 3d. Measurements showed that the average diameter of $NiFe_2O_4$–NG particles is approximately 80 nm. The particle size data obtained from TEM data are in very close agreement to the size calculated from the Debye–Scherrer method.

3. 3. FT-IR Characterization

Figure 4(a–d) shows the FTIR spectra of GO, NG, $NiFe_2O_4$ and $NiFe_2O_4$–NG. There are many O-containing groups that exist on GO sheets, such as hydroxyl, epoxy, and carboxyl groups. Majority of the O-containing groups will disappear after reduction. FTIR bands at 1050, 1220, 1405 and 1730 cm^{-1} were observed for GO. These bands correspond to C–O stretching, C–O–C stretching, O–H deformation vibration and C=O carbonyl stretching.[44] FTIR bands at 1400 cm^{-1} due to C=C stretching is observed in NG and the νC=O band at 1730 cm^{-1} completely disappeared due to reduction. The bands located at 1180 and 1565 cm^{-1} in Figure 4b are assigned to the ν C-N and ν C=C respectively. The FTIR spectra suggest N doping of GO. Figure 4 (c–d) shows the FT-IR bands of $NiFe_2O_4$ and $NiFe_2O_4$–NG. The bands observed in the range of 620–650 cm^{-1} corresponds to the intrinsic stretching vibrations of the M–O in the tetrahedral site. The second band around 3400–3500 cm^{-1} corresponds to O–H stretching vibrations.[45] Furthermore, it is observed that almost all the characteristic bands of oxygen containing functional groups (C=O, O–H, C–OH and C–O–C) disappeared in the FT-IR spectrum of $NiFe_2O_4$–NG depicting the change in the surface morpholgy of NG–$NiFe_2O_4$ composite. These findings show that $NiFe_2O_4$ nanoparticles are bonded to the NG. The results above show the heteroatom N was entered in the graphene structure and the $NiFe_2O_4$–NG composites was prepared favourably.

3. 4. Photocatalytic Measurements

The adsorption of light by the photocatalysts is the key feature of photocatalysis method. Figure 5a show the

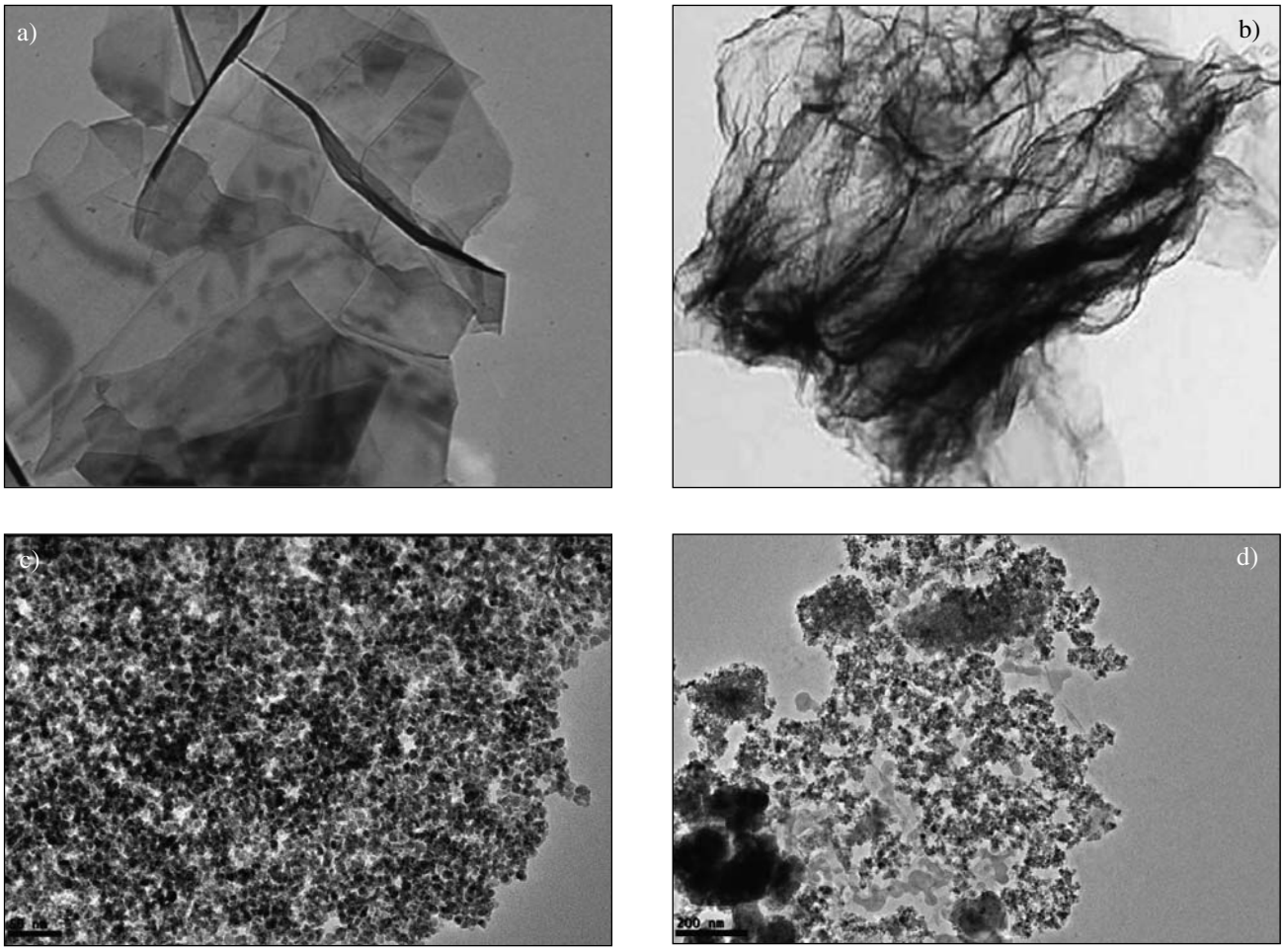

Figure 3. TEM images of (a) GO, (b) NG, (c) $NiFe_2O_4$ and (d) $NiFe_2O_4$–NG

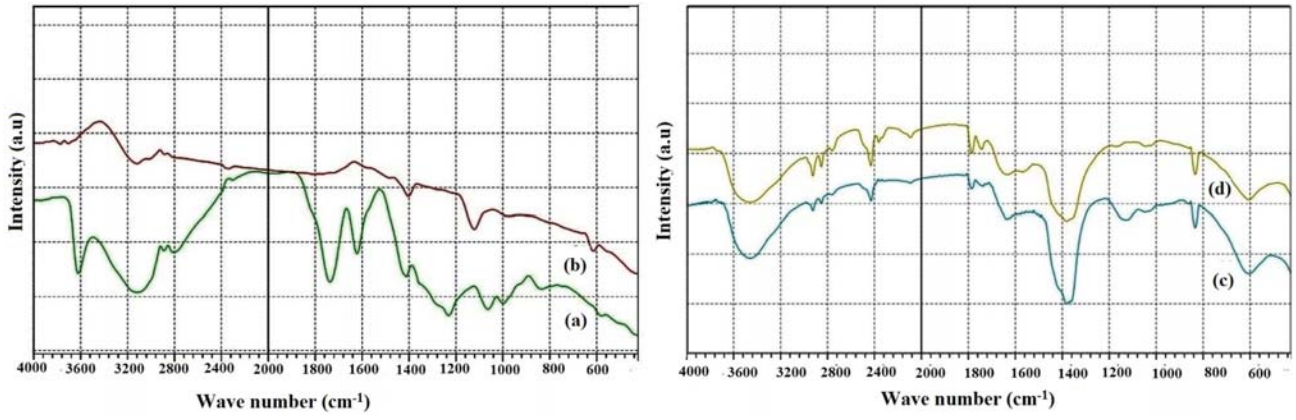

Figure 4. FT-IR spectra of (a) GO (b) NG (c) $NiFe_2O_4$ (d) $NiFe_2O_4$–NG

UV Spectrum of $NiFe_2O_4$–NG. The photocatalytic activities of the as-obtained $NiFe_2O_4$–NG nanocomposite photocatalysts were evaluated by monitoring the degradation of methylene blue (MB) under visible-light irradiation at 25 °C. Figure 5a shows the changes in the absorbance profiles of MB solution (concentration of MB, C = 0.075 M and path length, l = 1cm) in the presence of $NiFe_2O_4$–NG photocatalyst under visible-light irradiated at 25 °C recorded at different time intervals. The adsorption-desorption equilibriated solution of MB and $NiFe_2O_4$–NG was used

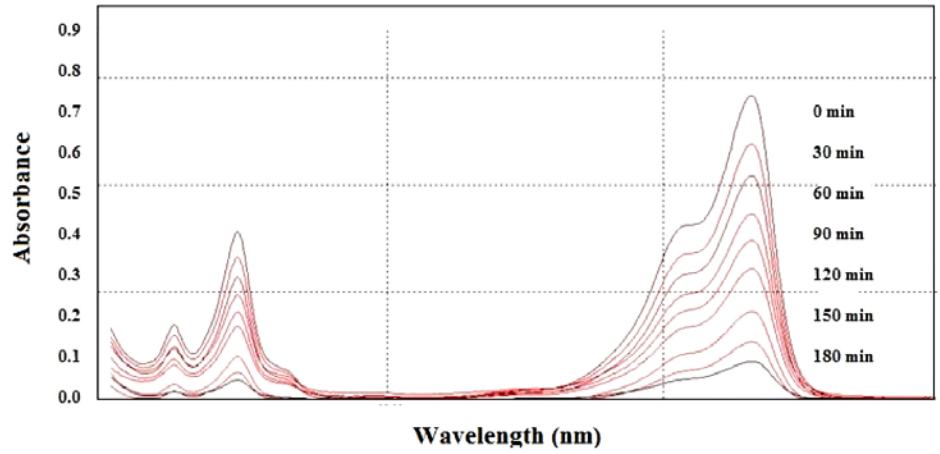

Figure 5a. Absorption spectra of the MB solution (C = 0.075 M and l = 1 cm) taken at different photocatalytic degradation times using $NiFe_2O_4$–NG.

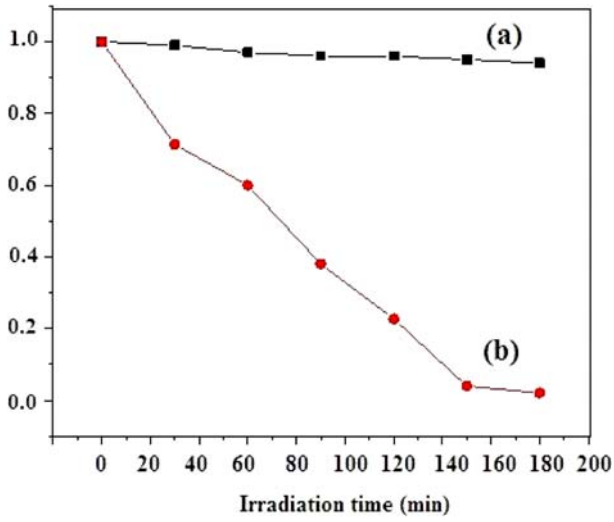

Figure 5b. Kinetics of photodegradation of (a) Pure MB and (b) the pure MB solution. The catalyst acts as magnetic material which gives good performance in magnetic separation for the $NiFe_2O_4$–NG photocatalysts using an external magnet.

3. 4. 1. Mechanism of Photocatalytic Activity Measurements

The photocatalytic activity for MB degradation can be best explained by the following mechanism. The notable increase in photocatalytic activity under visible light exposure can be attributed to exceptional synergistic effect between $NiFe_2O_4$ and the nitrogen-doped graphene sheets causing the effective separation of carriers generated by the light exposure in the $NiFe_2O_4$–NG composite system. A plausible mechanism for enhancement in photocatalysis process is shown as follows:

When the visible-light is irradiated on the surface of

$$NiFe_2O_4 + \text{Visible light} \longrightarrow NiFe_2O_4\,(h+e) \quad (2)$$

$$NiFe_2O_4\,(e) + \text{N-doped graphene} \longrightarrow NiFe_2O_4 + \text{N-doped graphene}\,(e) \quad (3)$$

$$\text{N-doped graphene}\,(e) + O_2 \longrightarrow O_2^{\cdot-} + \text{N-doped graphene} \quad (4)$$

$$NiFe_2O_4\,(h) + OH^- \longrightarrow NiFe_2O_4 + {}^{\cdot}OH \quad (5)$$

$$NiFe_2O_4\,(h) + {}^{\cdot}OH + O_2^{\cdot-} + C_{16}H_{18}ClN_3S(MB) \longrightarrow NiFe_2O_4 + CO_2 + H_2O + SO_4^{2-} + NO_3^- + Cl^- + NH_4^+ \quad (6)$$

as starting solution. In Figure 5b C/C_0 was plotted versus time where C_0 is initial concentration of methylene blue (0.075 M at time t = 0 min. and C is concentration at time t min.). It can be clearly seen that almost all the MB in the solution is decomposed after 180 min in presence of the $NiFe_2O_4$–NG while there is least photodegradation in $NiFe_2O_4$, the electron-hole pairs are formed (Eq. 2). Then by the percolation mechanism, the electrons generated by the photogeneration process are instantly transfer onto NG sheets (Eq. 3). Superoxide anion radical is produced from oxygen dissolved and activated through nitrogen doped graphene carrying negative charge (Eq. 4). The adsor-

bed water can react with holes to produce hydroxyl radical (Eq. 5). At the end superoxide anion, and hydroxyl radical cause the oxidation of MB dye adsorbed on the surface of $NiFe_2O_4$–NG composite by electrostatic interaction and π-π interaction between aromatic rings of methylene blue and graphene layer (Eq. 6). In the photocatalytic degradation process, the electrons of the photocatalyst i,e $NiFe_2O_4$–NG nanocomposite are excited from the valence band (VB) to the conduction band (CB) by the visible light irradiation. The photogenerated holes in the VB are scavenged by OH^- of water forming $^{\cdot}OH$ radicals which are responsible for the MB degradation process afterwards. The N-graphene performs two functions; (a) it acts as charge carrier to trap the delocalised electrons thereby restricting the (h–e) recombination. (b) Secondly, it increases the adsorption of MB dye on the catalyst surface thereby increasing the π-π interaction between aromatic rings of methylene blue and graphene layer.[46]

3. 5. Magnetic Characterization

Magnetization hysteresis loops of the as-prepared $NiFe_2O_4$ and $NiFe_2O_4$–NG samples at room temperature were measured using vibrating sample magnetometer as shown in Figure 6(a–b). The magnetic properties of the $NiFe_2O_4$ having inverse spinel structure can be described in terms of cations distribution. The magnetization originates from the Fe^{3+} ions at both tetrahedral and octahedral sites and Ni^{2+} is present only in octahedral sites.[47,48] Coercivity and saturation magnetization of $NiFe_2O_4$–NG are 47.4 G and 10.1 emu/g respectively, whereas that of $NiFe_2O_4$ are 33.5 G and 9.2 emu/g respectively. The values observed for $NiFe_2O_4$–NG are larger than those for $NiFe_2O_4$ which shows that $NiFe_2O_4$–NG is more easily separable than $NiFe_2O_4$. The increase in the saturation magnetization was possibly attributed to the increasing crystallinity and particle size of the nanoparticles.

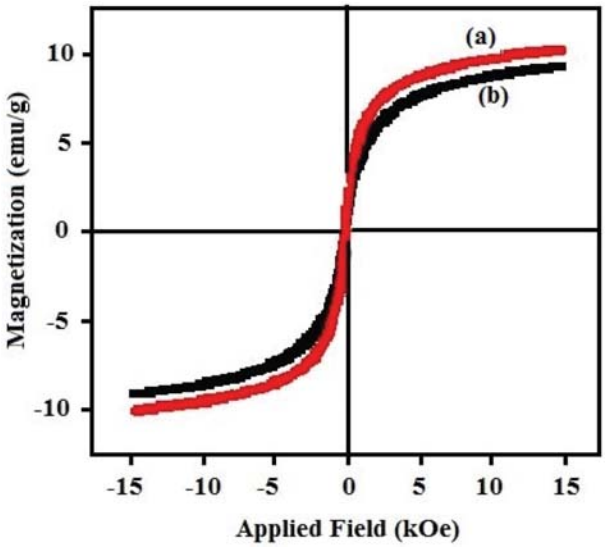

Figure 6. Magnetic hysteresis loop measured at 300 K for (a) $NiFe_2O_4$ (b) $NiFe_2O_4$–NG

4. Conclusions

In the outcome, a magnetic $NiFe_2O_4$–NG photocatalyst has been fabricated through hydrothermal route. The SEM and TEM images show that nitrogen-doped graphene sheets are flaked and furnished with $NiFe_2O_4$ nanoparticles having an average diameter of 80 nm. The photocatalytic activity measurements confirm that the $NiFe_2O_4$ nanoparticles combined with nitrogen-doped graphene sheets lead to exciting conversion of the inactive $NiFe_2O_4$ into very good catalyst for the degradation of methylene blue (MB) under visible light irradiation. The notable increase in photoactivity can be ascribed to the superior conductivity of the reduced NG sheets leading to favourable and efficient separation of photogenerated carriers (hole-electron) in the $NiFe_2O_4$–NG system. Subsequently, there is very large and useful change in photocatalytic activity after coupling nickel ferrite with nitrogen-doped graphene sheets.

5. Acknowledgements

We would like to acknowledge SAIF, Panjab University, Chandigarh and Indian Institute of Technology Guwahati for their technical support. We thank Indian Institute of Technology Mandi for powder X-ray diffraction study.

6. References

1. M. R. Hoffmann, S. T. Martin, W. Choi, D. W. Bahnemann, *Chem. Rev.* **1995**, 95, 69–96. https://doi.org/10.1021/cr00033a004
2. B. Mahrov, G. Boschloo, A. Hagfeldt, L. Dloczik, T. Dittrich, *Appl. Phys. Lett.* **2004**, 84, 5455–5457. https://doi.org/10.1063/1.1767961
3. A. Hattori, Y. Tokihisa, H. Tada, S. Ito, *J. Electrochem. Soc.* **2000**, 147, 2279–2283. https://doi.org/10.1149/1.1393521
4. G. K. Ropidas, M. Bohorquez, P. V. Kamat, *J. Phys. Chem.* **1990**, 94, 6435–6440. https://doi.org/10.1021/j100379a051
5. Z. J. Zhang, W. Z. Wang, W. Z. Yin, M. Shang, L. Wang, S. M. Sun, *Appl. Catal. B* **2010**, 10, 68–73. https://doi.org/10.1016/j.apcatb.2010.09.008
6. B. K. Vijayan, N. M. Dimitrijevic, J. S. Wu, K. A. Gray, *J. Phys. Chem. C* **2010**, 114, 21262–21269. https://doi.org/10.1021/jp108659a
7. X. Shu, J. He, D. Chen, *Ind. Eng. Chem. Res.* **2008**, 47, 4750–4753. https://doi.org/10.1021/ie071619d

8. K. S. Novoselov, A. K. Geim, S. V. Morozov, D. Jiang, Y. Zhang, S. V. Dubonos, I. V. Grigorieva, A. A. Firsov, *Science* **2004**, 306*,* 666–669. https://doi.org/10.1126/science.1102896
9. A. K. Geim, *Science* **2009**, 324, 1530–1534. https://doi.org/10.1126/science.1158877
10. S. Chen, J. Zhu, X. Wang, *ACS Nano* **2010**, 4, 6212–6218. https://doi.org/10.1021/nn101857y
11. Y. M. Li, X. J. Lv, J. Lu, J. Li, *J. Phys. Chem. C* **2010**, 114, 2177–21774.
12. O. Akhavan, *ACS Nano* **2010**, 4, 4174–4180. https://doi.org/10.1021/nn1007429
13. K. S. Novoselov, A. K. Geim, S. V. Morozov, D. Jiang, M. I. Katsnelson, I. V. Grigorieva, S. V. Dubonos, A. A. Firsov, *Nature* **2005**, 438, 197–200. https://doi.org/10.1038/nature04233
14. J. Sakamoto, J. van Heijst, O. Lukin, A. D. Schluter, *Angew. Chem. Int. Ed.* **2009**, 48, 1030–1069. https://doi.org/10.1002/anie.200801863
15. M. Burghard, H. Klauk, K. Kern, *Adv. Mater.* **2009**, 21, 2586–2600. https://doi.org/10.1002/adma.200803582
16. R. Devi, G. Prabhavathi, R. Yamuna, S. Ramakrishanan, N. K. Kothurkar, *J. Chem. Sci.* **2014**, 126, 75–83. https://doi.org/10.1007/s12039-013-0536-1
17. H. Zhang, X. Lv, Y. Li, Y. Wang, J. Li, *ACS Nano* **2010**, 4, 380–386. https://doi.org/10.1021/nn901221k
18. G. Williams, B. Seger, P. V. Kamat, *ACS Nano* **2008**, 2, 1487–1491. https://doi.org/10.1021/nn800251f
19. Y. Zhang, Z. R. Tang, X. Fu, Y. J. Xu, *ACS Nano* **2010,** 4, 7303–7314. https://doi.org/10.1021/nn1024219
20. D. H. Yoo, V. C. Tran, V. H. Pham, J. S. Chung, N. T. Khoa, E. J. Kim, S. H. Hahn, *Curr. Appl. Phys.* **2011**, 11, 805–808. https://doi.org/10.1016/j.cap.2010.11.077
21. O. Akhavan, *Carbon* **2011**, 49, 11–18. https://doi.org/10.1016/j.carbon.2010.08.030
22. T. G. Xu, L. W. Zhang, H. Y. Cheng, Y. F. Zhu, *Appl. Catal. B* **2011**, 101, 382–387. https://doi.org/10.1016/j.apcatb.2010.10.007
23. S. Shylesh, V. Schunemann, W. R. Thiel, *Angew. Chem. Int. Ed.* **2010**, 49, 3428–3459. https://doi.org/10.1002/anie.200905684
24. H. Zhang, S. Gao, N. Shang, C. Wang, Z. Wang, *RSC Adv.* **2014**, 4, 31328–31332.
25. N. Velinov, K. Koleva, T. Tsoncheva, D. Paneva, E. Manova, K. Tenchev, B. Kunev, I. Genova, I. Mitov, *Cent. Eur. J. Chem.* **2014,** 12, 250–259. https://doi.org/10.2478/s11532-013-0371-8
26. B. I. Kharisov, H. V. R. Dias, O. V. Kharissova, *A. J. Chem.* **2014,** DOI: 10.1016/j.arabjc.2014.10.049. https://doi.org/10.1016/j.arabjc.2014.10.049
27. Y. Fu, Q. Chen, M. He, Y. Wan, X. Sun, H. Xia, X. Wang, *Ind. Eng. Chem. Res.* **2012**, 51, 11700–11709. https://doi.org/10.1021/ie301347j
28. C. U. Aniz, T. D. R. Nair, *OJPC*, **2011**, 1, 124–130. https://doi.org/10.4236/ojpc.2011.13017
29. N. Rezlescu, E. Rezlescu, P. D. Popa, C. Doroftei, M. Ignat, *Romanian Reports in Physics*, **2013,** 65, 1348–1356.
30. Y. Kinemuchi, K. Ishizaka, H. Suematsu, W. H. Jiang, K. Yatsui, *Thin Solid Films* **2002**, 407, 109–113. https://doi.org/10.1016/S0040-6090(02)00021-4
31. Y. S. Chung, S. B. Park, D. W. Kang, *Mater. Chem. Phys.* **2004**, 86, 375–381. https://doi.org/10.1016/j.matchemphys.2004.03.027
32. Rahmayeni, S. Arief, Y. Stiadi, R. Rizal, Zulhadjri, *Indo. J. Chem.* **2012**, 12, 229–234.
33. Y. S. Fu, X. Wang, *Ind. Eng. Chem. Res.* **2011**, 50, 7210–7218. https://doi.org/10.1021/ie200162a
34. H. Guo, Q. Gao, *J. Power Sources* **2009**, 186, 551–556. https://doi.org/10.1016/j.jpowsour.2008.10.024
35. L. Zhao, L. Fan, M. Zhou, H. Guan, S. Qiao, M. Antonietti, M. Titirici, *Adv. Mater.* **2010**, 22, 5202–5206. https://doi.org/10.1002/adma.201002647
36. L. Chen, X. Zhang, H. Liang, M. Kong, Q. Guan, P. Chen, Z. Wu, S. Yu, *ACS Nano* **2012**, 6, 7092–7102. https://doi.org/10.1021/nn302147s
37. J. Xu, G. Dong, C. Jin, M. Huang, L. Guan, *ChemSusChem* **2013**, 6*,* 493–499. https://doi.org/10.1002/cssc.201200564
38. S. Bag, C. R. Raj, *J. Chem. Sci.* **2016**, 128, 339–347. https://doi.org/10.1007/s12039-016-1034-z
39. W. S. Hummers R. E. Offeman *J. Am. Chem. Soc.* 80 (1958) 1339–1339. https://doi.org/10.1021/ja01539a017
40. A. I. Vogel, A Textbook of Quantitative Inorganic Analysis, forth ed., Longman, London, **1978**.
41. D. C. Marcano, D. V. Kosynkin, J. M. Berlin, A. Sinitskii, Z. Sun, A. Slesarev, L. B. Alemany, W. Lu, J. M. Tour, *ACS Nano* **2010**, 4, 4806–4814. https://doi.org/10.1021/nn1006368
42. Y. Fu, H. Chen, X. Sun, X. Wang, *AIChE J.* **2012**, 58, 3298–3305. https://doi.org/10.1002/aic.13716
43. X. Zheng, Q. Xu, L. He, N. Yu, S. Wang, Z. Chen, *J. Phys. Chem. B* **2011**, 115, 5815–5826. https://doi.org/10.1021/jp2018082
44. M. Acik, C. Mattevi, C. Gong, G. Lee, K. Cho, M. Chhowalla, *ACS Nano* **2010**, 10, 5861–5868. https://doi.org/10.1021/nn101844t
45. D. Du, P. Li, J. Ouyang, *ACS Appl. Mater. Interfaces* **2015**, 7, 26952–26958. https://doi.org/10.1021/acsami.5b07757
46. L. Gan, L. Xu, S. Shang, X. Zhou, L. Meng, *Ceram. Int.* **2016,** 42, 15235–15241. https://doi.org/10.1016/j.ceramint.2016.06.160
47. H. Nathani, S. Gubbala, R. D. K. Misra, *Mater. Sci. Eng. B* **2005,** 121, 126–136. https://doi.org/10.1016/j.mseb.2005.03.016
48. A. B. Nawale, N. S. Kanhe, K. R. Patil, S. V. Bhoraskar, V. L. Mathe, A. K. Das, *J Alloys Compd.* **2011**, 509, 4404–4413. https://doi.org/10.1016/j.jallcom.2011.01.057

Povzetek

Preprost sintezni način smo uporabili za pripravo magnetnega fotokatalizatorja $NiFe_2O_4$ na grafenu, dopiranem z dušikom (NG). Kompozit $NiFe_2O_4$–NG smo pripravili z enostopenjsko hidrotermalno sintezo. Nanokompozitni katalizator smo karakterizirali z naslednjimi metodami: rentgensko praškovno difrakcijo (XRD), vrstično elektronsko mikroskopijo (SEM), presevno elektronsko mikroskopijo (TEM), infrardečo spektroskopijo (FT-IR), UV-Vis spektroskopijo in magnetometrijo z vibrirajočim vzorcem (VSM). Kombinacija nanodelcev $NiFe_2O_4$ in grafena, dopiranega z dušikom pretvori $NiFe_2O_4$ v dober katalizator za fotokatalitični razpad barvila metilen modro (MB). Fotokatalitično aktivnost pod vplivom vidne svetlobe lahko pripišemo obsežnemu premiku vzbujenih elektronov iz $NiFe_2O_4$ v prevodni pas reduciranega grafena (NG). Že sami nanodelci $NiFe_2O_4$ imajo takšne magnetne lastnosti, da jih lahko uporabimo za magnetno separacijo v raztopini brez dodatne uporabe magneta.